ACS OMEGA

http://pubs.acs.org/journal/acsodf

Article

Novel Approaches of Nanoceria with Magnetic, Photoluminescent, and Gas-Sensing Properties

Leandro S.R. Rocha,* Rafael A.C. Amoresi, Henrique Moreno, Miguel A. Ramirez, Miguel A. Ponce, Cesar R. Foschini, Elson Longo, and Alexandre Z. Simões

Cite This: *ACS Omega* 2020, 5, 14879−14889

Read Online

ACCESS | Metrics & More | Article Recommendations

ABSTRACT: The modification of CeO_2 with rare-earth elements opens up a wide range of applications as biomedical devices using infrared emission as well as magnetic and gas-sensing devices, once the structural, morphological, photoluminescent, magnetic, electric, and gas-sensing properties of these systems are strongly correlated to quantum electronic transitions between rare-earth f-states among defective species. Quantitative phase analysis revealed that the nanopowders are free from secondary phases and crystallize in the fluorite-type cubic structure. Magnetic coercive field measurements on the powders indicate that the substitution of cerium with lanthanum (8 wt %), in a fluorite-type cubic structure, created oxygen vacancies and led to a decrease in the fraction of Ce species in the 3+ state, resulting in a stronger room-temperature ferromagnetic response along with high coercivity (160 Oe). In addition to the magnetic and photoluminescent behavior, a fast response time (5.5 s) was observed after CO exposure, indicating that the defective structure of ceria-based materials corresponds to the key of success in terms of applications using photoluminescent, magnetic, or electrical behaviors.

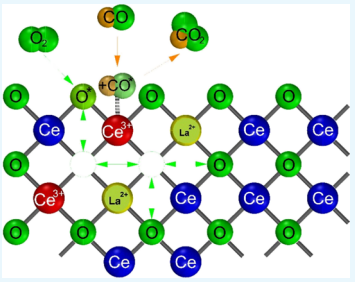

1. INTRODUCTION

The wide theoretical energy gap (E_g = 6.0 eV), high dielectric constant ($\varepsilon \approx 23$), and low dielectric loss ($\tan \delta \approx 0.0064$ at 7 GHz)[1,2] of Ceria (cerium oxide, CeO_2) makes it one of reactive rare earth oxides. However, experimentally its energy gap value is close to 3.2 eV because of O (2p) → Ce (4f) transitions, a mechanism yet to be fully uncovered.[3,4] Different methods have been applied for synthesizing CeO_2 crystals, such as: co-precipitation,[5] flow method,[6] organometallic decomposition,[7] and sol−gel methods.[8] The conventional hydrothermal and microwave-assisted hydrothermal (MAH) represent alternatives to these preparation routes, which allow for the synthesis of pure oxides at low-temperature conditions (below 200 °C), leading to lower processing times and associated energy cost.[9,10]

It is well known that the properties of ceria-based materials depend on the reduction of Ce^{4+} to Ce^{3+} species. Dhara et al.[11] showed a blue-shift in the absorption spectrum of CeO_2 nanocrystals, owing to the charge transfer mechanism between O (2p) and Ce (4f) states. Additionally, Abbas et al.[12] showed that the narrowing of the band gap could also be achieved by increasing the number of oxygen vacancies in the structure by systematically doping CeO_2 nanoparticles, synthesized by the co-precipitation method Mn. Liu et al.[13] reported size-dependent ferromagnetism (FM) in CeO_2 powders synthesized by the precipitation route, with a ferromagnetic saturation ($M_s \approx 0.08$ emu/g) only observed in powders with average particle size smaller than 20 nm. Similarly, Chen et al.[14] reported room-temperature FM (RT-FM) in CeO_2 nanoparticles prepared by the thermal decomposition method ($M_s \approx 0.12$ emu/g). According to literature, oxygen vacancies at the surface are created because of exchange interactions between electron spin moments, owing to the high surface-to-volume ratio, which is associated with the observed FM.[15] Recent combined systematic spectroscopy and microscopic analysis[16] demonstrated that differences in electron position are strongly correlated to the magnetic behavior, with two types of electron localization revealed, both resulting in the reduction of the Ce(IV) species. One is located at the Ce atom adjacent to oxygen vacancies, responsible for the hopping conduction mechanism, while the other distributes at farther shell playing the major role in FM. This behavior indicates that the presence of oxygen vacancies is essential for the formation of FM in CeO_2. In this context, nanocrystalline ceria emerged because of its particular physicochemical properties, with the most significant differences between nano and bulk materials attributed to the extremely high specific surface area because of size effects and quantum confinement.[17−21] The unique combination of properties of Ceria-based ceramics makes it

Received: December 11, 2019
Accepted: February 28, 2020
Published: June 15, 2020

https://dx.doi.org/10.1021/acsomega.9b04250
ACS Omega 2020, 5, 14879−14889

an important multifunctional material with a wide range of applications, such as catalysts, photocatalysts, solar cells, solid oxide fuel cells, hydrogen storage materials, oxygen permeation membranes, optical devices, ultraviolet absorber, polishing materials, and in the environmental sensing field.[22−32] Novel approaches have been employed for the preparation of ultra-highly sensitive devices using surface acoustic wave sensors, which enable detection with the sub-ppb limit.[33−35]

With the increasing concern regarding the numerous cases of carbon monoxide (CO) poisoning[36] and the increase of indoor air pollutants, the development of more reliable, efficient, and low cost gas sensors has become a major driving force for scientists around the world. Oxide semiconductors appear to be a suitable choice for gas-sensing devices because of some unique properties, such as high selectivity, sensitivity, stability, and reversibility[37,38] but also low cost, durability, and low power consumption. We also must consider other important parameters such fast response, reduced dimensions, portability, and real-time detection.[39] The microstructure plays a significant role in improving the sensitivity of sensors. Composition, surface modification, temperature, and humidity are also important factors.[40,41] Maekawa et al.[42] determined that sensitivity and selectivity to gases depend strongly on the grain size, and that the presence of larger grains improves selectivity. Moreover, the parameters of the electron-depletion regions within the structure of the material help explain the sensing mechanism. The oxygen present in the atmosphere adsorbs on the surface and capture electrons from the conduction band (CB)[43,44] to form anionic oxygen species, depending on the working temperature. These electrons become trapped on the surface, creating the electron-depleted region and hence decreasing the conductivity of the sensor. Finally, the adsorbed oxygen species oxidizes CO to form carbon dioxide (CO_2), leading to an increase in conductivity,[45] which represents the response of the sensor.

Besides the technological progresses in gas-sensing materials, several improvements must be achieved. In previous works, our group optimized the synthesis of CeO_2 nanoparticles and thick films through the MAH method for pure and rare earth-doped CeO_2,[46] showing the strong influence of lanthanum modification on the redox (Ce^{3+}/Ce^{4+}) capability. Additionally, we showed that a 8 wt % La-doped CeO_2 sample presented a significant dual sensing behavior when exposed to CO, with a response-time (tresp) of approximately 5 s and a reversibly optical reply close to 0.3 s, changing its surface color, close to 400 °C. This effect is intrinsically related to ferromagnetic,[47] photoluminescent,[48] and gas-sensing properties. Additionally, the electrical conduction of CeO_2 films is virtually dominated by cluster-to-cluster charge transfer (CCCT) processes,[49] indicating an electron quantum tunneling/hopping mechanism on the film response, which stems from interaction between intrinsic vacancies among the clusters, such as $[CeO_8]_O'...[CeO_7{\cdot}V_O^{\bullet\bullet}]...[CeO_8]_O'$, which can still be present even above room temperature.[50]

Thus, as a natural extension of the previous published work,[46] a combined investigation of pure and lanthanum-doped CeO_2 sphere-like nanostructures and thick films was performed, highlighting the interplay between the magnetic, photoluminescent, and gas-sensing behaviors after CO exposure.

2. RESULTS AND DISCUSSION

2.1. Characterization of the CeO_2 Nanoparticles.

2.1.1. X-ray Diffraction and Rietveld Refinement. Figure 1a,b illustrates the X-ray diffraction (XRD) patterns of pure

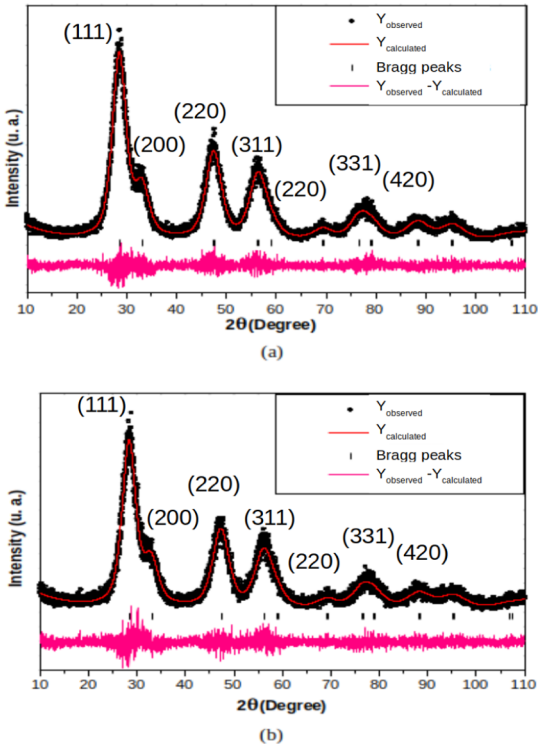

Figure 1. Rietveld refinement of pure (a,b) La-doped CeO_2 nanopowders.

and lanthanum-doped samples, respectively. Both patterns exhibit peaks that consistently correspond to the face-centered cubic fluorite-type structure of cerium oxide, with a space group $Fm\bar{3}m$, according to the Joint Committee on Powder Diffraction Standards (JCPDS) 34-0394 data-set. This indicates that pure CeO_2 was successfully synthesized via this procedure. By analyzing the diffracted peaks of the La-doped CeO_2 sample, shown in Figure 1b, a widening of the peaks related to the crystallographic planes (111) and (220) is observed at 2θ at 28 and 48, respectively, compared to the pure sample. This is because of the incorporation of La atoms in the place of Ce, causing symmetry and disorder changes in the crystallite upon insertion of rare earth.

The XRD patterns were analyzed by Rietveld refinement. The employed method indicates a good fit between the calculated and experimentally obtained patterns, which is supported by the statistical parameters R bragg, R_{wp}, and R_{exp} (Table 1).

GoF values evidence that the refinement is in agreement with what has been released in the literature, along with the both experimentally measured lattice parameter (a) and unit cell volumes, very close to the PDF card (JCPDS 34-0394) for CeO_2 powder in which $a \approx 5.4165$ Å.[51−53] These values can be affected by processing temperature and time, heating rate, and solvents, which directly influences the formation of $[CeO_8]$ rare-earth clusters within the cubic fluorite structure. Furthermore, they control the occurrence of structural defects, such as oxygen vacancies. Slightly larger lattice parameter and

https://dx.doi.org/10.1021/acsomega.9b04250
ACS Omega 2020, 5, 14879−14889

Table 1. Rietveld Refinement Parameters for the Pure and Lanthanum-Doped CeO_2 Nanopowders

	lattice parameters						
refined formula ($Ce_{1-(3/4)x}La_xO_2$)	$a = b = c$ (Å)	$\alpha = \beta = \gamma$	unit cell volume (Å^3)	R_B (%)	GoF (%)	R_{wp} (%)	R_{exp} (%)
X = 0.00	5.4134 (6)	90	158.64 (6)	3.06	1.05	12.18	9.04
X = 0.08	5.4165 (9)	90	158.91 (8)	4.56	1.05	15.42	11.3

volumes are seen for the doped sample in comparison to the pure sample (Table 1), in accordance to literature.[52] In addition to the refinement, the crystallite size (d) was calculated using Debye Scherrer's equation. The calculated values were of 16.57 and 10.42 nm for the pure and La-doped CeO_2 samples, respectively, which evidences the successful incorporation of dopant species into the host structure. It is known that rare earth-doped ceria could create a corresponding number of anion vacancies, resulting in a solid solution with high ionic conductivity and defective surfaces, which may enhance its redox properties. Besides, lanthanum prevents the growth of ceria crystallites in severe oxidizing environments, as it happened in this case, acting as a stabilizer.[54]

Additionally, according to the previously referenced CCCT mechanism as well as to the small polaron theory,[55] the probability of electron tunneling/hopping transitions is roughly dependent on the distance between two adjacent sites, and small variations on these certainly influence their quantum probability of transference among defective clusters throughout the bulk. Furthermore, these variables can increase or reduce the occurrence of structural defects, such as oxygen vacancies, playing a major role in these mechanisms.

2.1.2. Transmission Electron Microscopy. The size and morphology of the pure and La-doped CeO_2 nanoparticles were analyzed using transmission electron microscopy (TEM), shown in Figure 2, which reveals that the MAH product consists of unevenly dispersed quasi-spherical nanostructured particles with sizes around 10 nm, approximate to the measured average crystallite sizes (d) of 16.57 and 10.42 nm for the pure and doped samples, respectively.

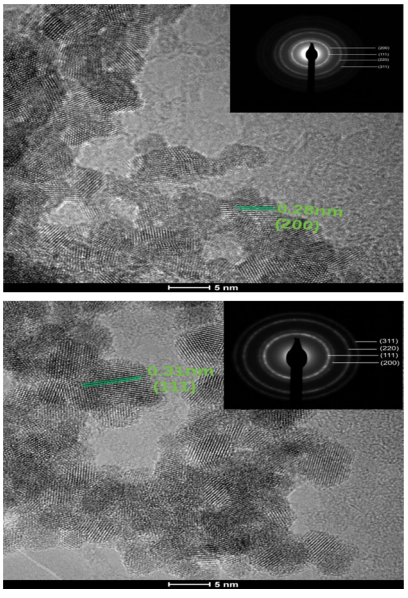

Figure 2. TEM and SAED micrographs of (a) pure and (b) La-doped CeO_2 nanoparticles.

Both powder samples presented a formation of agglomeration, owing to the van der Waals forces, which is an indicative of ultra-fine particles. In order to minimize their surface energy, the particles have a tendency to form agglomerates, with a minimum surface-to-volume ratio,[56] explaining why the particles agglomerate, although matching the interplanar space of the (111) and (200) fringes of a fluorite cubic structure. The nanocrystallinity and crystallography of the samples are proven by selected area electron diffraction analysis (SAED). SAED patterns are shown as insets of Figure 2a,b and exhibits four broad rings with *d*-spacing, which can be attributed to (111), (200), (220), and (311) reflections of the fluorite cubic structure. The ring patterns obtained from the SAED confirm the high purity, nanocrystallinity, and the fluorite-type structure of the pure and lanthanum-doped samples, reassuring the formation of highly crystalline materials.

2.1.3. Magnetic Properties. Magnetization (M) versus magnetic field (H) loops were recorded for pure and La-doped CeO_2 samples at 300 K, shown in Figure 3. The corresponding values of magnetization and coercive fields are shown in Table 2.

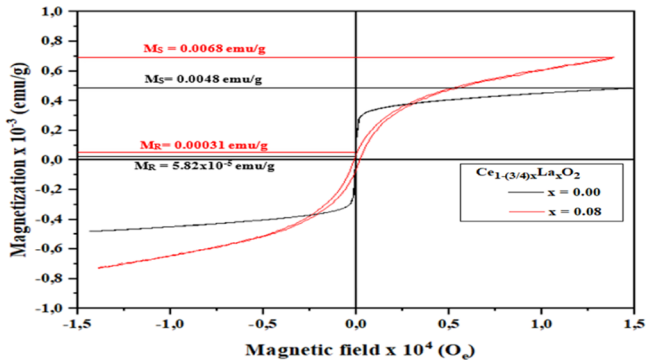

Figure 3. Magnetization vs applied field of pure and La-doped CeO_2 nanoparticles.

Table 2. Magnetic Saturation, Reminiscent Magnetization, and Coercivity

	$Ce_{1-(3/4)x}La_xO_2$				
sample	M_S (emu/g)	M_R (emu/g)	H_c (Oe)	Φ (nm)	d (nm)
X = 0.0	4.8×10^{-3}	5.82×10^{-5}	0.00	12	16.57
X = 0.08	6.8×10^{-3}	3.10×10^{-4}	160.00	6	10.42

Both samples show weak RT-FM. However, La-doping causes an increase in both residual (M_R) and saturation magnetization (M_S) values (as listed in Table 2), in accordance with the generation of more ferromagnetic defective species after the modification with rare-earth elements,[57,58] and higher than the reported M_s for pure CeO_2 nanospheres.[14,59] In addition, the magnetic susceptibility (c_i) decreases significantly on the La-doped CeO_2 sample in comparison to the pure sample, which is evidenced by the decrease in the initial slope

https://dx.doi.org/10.1021/acsomega.9b04250
ACS Omega 2020, 5, 14879−14889

on the $M-H$ curve (when $H = 0$). Sundaresan et al.[59] reported CeO_2 nanoparticles with an average size of approximately 15 nm, showing RT-FM with an $M_s = 1.9 \times 10^{-3}$ emu/g, while ours were 4.8 and 6.8×10^{-3} emu/g. We can also see a strong increase in coercivity (from 0 to 160 Oe or 0.016 T) for the L.D.C sample, 8 times higher than Ni-doped CeO_2 nanoparticles presented.[60] The results obtained here provide evidence that the La-doped CeO_2 sample can indeed raise the magnetic moment because of the presence of more oxygen vacancies in the structure, with the consequent generation of a direct ferromagnetic coupling called F-center exchange (FCE)[61] on neighboring Ce species,[62] owing to the presence of both variable valence states (Ce^{4+}/Ce^{3+}) as well as to oxygen vacancies. Additionally, the particle size has been reported to influence the magnetic properties of materials. Here, the crystallite size is quite small (~10 nm), leading to the uncompensated existence of exchanged-interacted spins at the crystallite surface responsible for the observed ferromagnetic behavior.[63]

2.2. Characterization of Thick Films. Because the dual sensing properties have a high predominance in the CeO_2 sample after La modification,[46] the correlation between the short-range structural order, electronic, and sensor effects was only made for the La-doped CeO_2 system before and after atmosphere exposure.

2.2.1. Raman Spectroscopy. The Raman spectra of the rare earth-doped film before and after CO exposure (Figure 4)

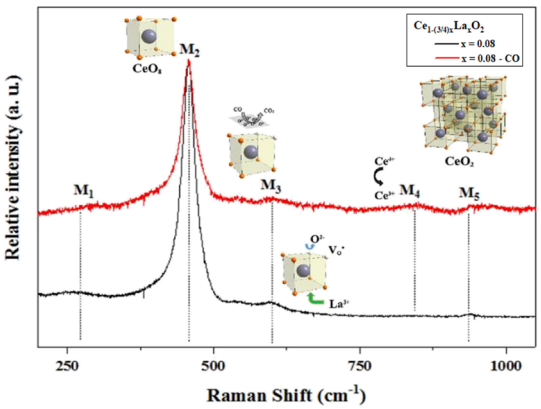

Figure 4. Raman spectroscopy of the La-doped film before and after CO exposure.

show the presence of five modes (M_1-M_5). Near 260 cm^{-1}, the M_1 is associated with a transversely acoustic mode.[64] The M_2 mode at 465 cm^{-1} represents the typical F_{2g} (M_2) symmetric vibrational mode associated to the cubic fluorite structure of ceria. The low-intensity M_3 mode (600 cm^{-1}) indicates the formation of oxygen vacancies as a result of the incorporation of La^{3+} species into the CeO_2 structure, while the vibrational mode M_4 indicates the reduction of Ce^{4+} to Ce^{3+}.[65−67] Close to 960 cm^{-1}, a fifth mode (M_5) is detected, related to the transverse optic mode.[68] The purge of CO resulted in the reduction of M_1, M_2, and M_3 intensities along with the appearance of M_4 mode, which indicates an alteration of the short-range order symmetry with reduction of Ce^{4+} to Ce^{3+} species, and an increase in the concentration of oxygen-related defects within the structure of the material,[69] corroborating with the magnetic behavior increase.

The symmetric breathing mode of the O atoms around each cation is linked to the main Raman peak (F_{2g}) near 450 cm^{-1}, which is nearly independent of the cation mass because only the O atoms move.[70] According to the literature,[64] cubic fluorite structure cerium oxide has Raman-active threefold-degenerate F_{2g} mode at ~465 cm^{-1} shifts, which broadens with decreasing particle size. For ceria nanoparticles prepared by the microwave-assisted solvothermal route,[71] with a narrow particle size distribution (2−4 nm), there is a peak shift to lower frequencies. This effect is a result of lattice expansion with decreasing particle size. The same shift to lower frequencies was observed on gadolinium- and lanthanum-doped ceria.[72,73]

2.2.2. Gas-Sensing Properties. Figure 5 illustrates the relative resistance versus temperature curve for the La-doped

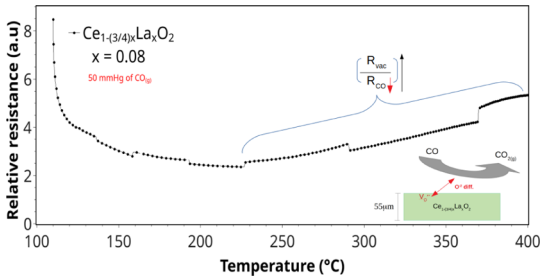

Figure 5. Relative resistance × temperature (°C) of the La-doped CeO_2 thick film at 50 mmHg of $CO_{(g)}$.

CeO_2 thick film, measured as a function of R_{vac}/R_{gas}, where R_{gas} corresponds to the resistance of the films when they reach an equilibrium state after CO exposure, and R_{vac} corresponds to the resistance of films when in vacuum. The sample presented a similar behavior of n-type semiconductor materials when in contact with reducing atmospheres,[74] responsible for the injection of electrons toward the bulk along with the consequent reduction in resistance (R_{CO}). The maximum response for the system can be seen around 400 °C, with a relative resistance of ~4, being close to the working temperature values reported for carbon monoxide ceria-based sensors, around 300−500 °C with a 500 ppm detection limit[75] as well as to the ceria quantum dot-based films with a working temperature of 400 °C.[76]

After determining the working temperature, the resistance versus time (Figure 6) behavior was studied at 400 °C, changing the atmosphere from vacuum to synthetic air (~20% oxygen) and 50 mmHg of CO (99.99%). Particularly, a relatively fast response time of 5.5 s can be observed after CO

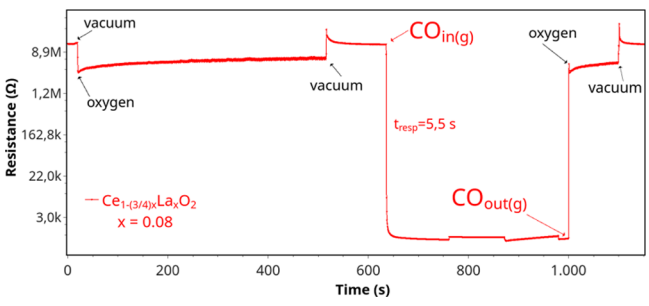

Figure 6. Relative resistance × time (s) for the La-doped CeO_2 thick film under exposure to gaseous atmospheres.

https://dx.doi.org/10.1021/acsomega.9b04250
ACS Omega 2020, 5, 14879−14889

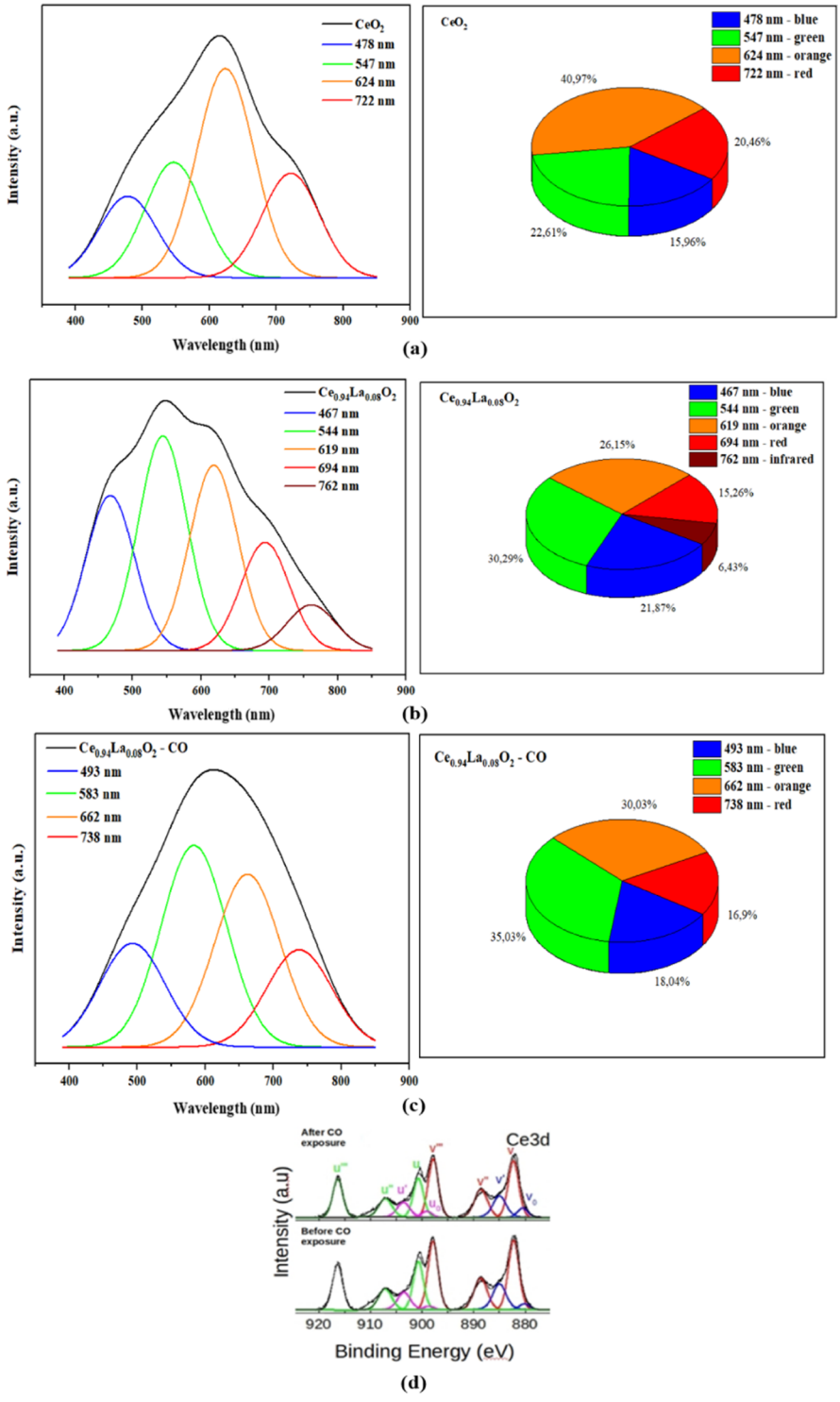

Figure 7. PL response of the (a) pure and La-doped CeO_2 thick films before (b) and after (c) CO exposure. (d) Depicts the Ce 3d XPS spectra.

exposure, slightly higher than the 2 s obtained with a sintered CeO_2 film at 950 °C[77] but better than the 9 s reported by López-Mena et al.[78] with 300 °C-calcined films. The observed resistance decrease indicates an n-type semiconductor behavior of the doped material. When the film is exposed to CO, Ce^{4+} clusters, such as $[CeO_8]^{\times}$, $[CeO_7{\cdot}V_O^{\times}]$, and $[CeO_7{\cdot}V_O^{\bullet}]$, reduce to Ce^{3+}, represented by $[CeO_8]'_O$ clusters, as a consequence of the transient $4f^1$ electrons. These electrons migrate between clusters by the CCCT mechanism (hopping/tunneling), owing to polarons, with a probability that roughly depends on the distance between adjacent sites. This charge transfer between polarons is intrinsically created by the redox process of $Ce^{3+} \leftrightarrow Ce^{4+}$, according to the exposed atmosphere. Considering the electrical conduction controlled by the CCCT mechanism, during CO exposure, in which the oxygen vacancies play the major role, the energy between the Fermi level and the 4f state moves in order to generate charge compensation, changing the number of electrons available for conduction. In previous works, we realized that the temperature where the CO-sensing response takes place is greater than 250 °C.[46] Additionally, it

https://dx.doi.org/10.1021/acsomega.9b04250
ACS Omega 2020, 5, 14879−14889

was shown that prior exposure to $CO_{(g)}$ at 400 °C raised the amount of oxygen vacant sites. This interaction between the gas and the film surface must be established considering the reaction with the previous adsorbed oxygen species onto the CeO_2 surface, according to the following equation

$$2CO + O_{2(ads)}^{-} \rightarrow 2CO_2 + e^{-} \qquad (T < 100\ ^\circ C) \tag{1}$$

In terms of intrinsic defective clusters and the charge transfer process among them, the above equation can be represented as

$$[CeO_7 \cdot V_O^{\bullet}]...O'_{2(ads)} + 2CO \rightarrow [CeO_7 \cdot V_O^{\times}] + 2CO_2 \qquad (T < 100\ ^\circ C) \tag{2}$$

of which do not influence in the overall sample resistance. Increasing the working temperature, we have the following situation

$$CO + O^{-} \rightarrow CO_2 + e^{-} \qquad (T > 100\ ^\circ C) \tag{3}$$

or, represented by clusters, as

$$[CeO_7 \cdot V_O^{\bullet}]...O'_{(ads)} + CO \rightarrow [CeO_7 \cdot V_O^{\times}] + CO_2 \tag{4}$$

After oxygen removal from the surface, as a consequence of the previous reactions, or when samples are exposed to a vacuum atmosphere, then CO interacts directly with the clusters

$$[CeO_8]...[CeO_7 \cdot V_O^{\bullet}]...CO_{(ads)} \rightarrow [CeO_8]'...[CeO_6 \cdot 2V_O^{\bullet\bullet}] + CO_2 \tag{5}$$

$$[CeO_8]_O^{\times}...[CeO_8]_d^{\times}...[CeO_7 \cdot V_O^{\times}]...CO_{(ads)} \rightarrow [CeO_8]'...[CeO_6 \cdot 2V_O^{\bullet}]...[CeO_8]' + CO_2 \tag{6}$$

$$[CeO_8]_O...[CeO_8]_d...CO_{(ads)} \rightarrow [CeO_8]'...[CeO_7 \cdot V_O^{\bullet}] + CO_2 \tag{7}$$

$$[CeO_8]_O...[CeO_8]_d...[CeO_8]_O...CO_{(ads)} \rightarrow [CeO_8]'...[CeO_7 \cdot V_O^{\bullet\bullet}]...[CeO_8]' + CO_2 \tag{8}$$

The influence of temperature on reactions with CO was previously considered by Lv et al.[47] The CCCT mechanism can also be expressed after CO exposure, according to these equations, where the electron situated in adsorbed oxygen species onto the surface returns to the system, reducing the cluster from $[CeO_7 \cdot V_O^{\bullet}]$ to $[CeO_7 \cdot V_O^{\times}]$, with a consequent decrease of the electrical resistance. We can observe that when CO reacts at the surface, two electrons become available for conduction through Ce $4f^1$ states, thus increasing the number of Ce^{3+} species ($[CeO_8]'_O$) on the right side of the equation, with the consequent decrease in resistance, as seen in Figure 6.

2.2.3. Photoluminescent Response. Because we have not reported the photoluminescence (PL) behavior of the pure sample before, we also have considered this system in this section.

Therefore, in order to better understand the effect of CO on the nature of defects along with their influence on the sensing behavior of the semiconductor thick film when a trivalent cation (La^{3+}) is introduced in the CeO_2 structure, the PL response of the film was measured. Doping of cerium oxide can intensify the dynamics of charge transfer and the formation of permanent dipoles modifying the photoluminescent properties of this oxide. Figure 7a–c shows the PL emission of the pure film (a) and La-doped film before (b) and after CO exposure (c), respectively. Usually, the PL emission for semiconductor oxides is related to defects in the crystalline structure mainly with the presence of oxygen vacancies, causing charge transfer because of the presence of additional energetic levels within the band gap region.[79] Defects are classified according to the energy levels created between the valence (VB) and CB bands. Shallow defects are those located near to the edges of VB or CB, causing emissions in the more energetic region, blue.[80] Deep defects are at the energy levels farther away from VB and CB edges, resulting in emissions in less energetic regions, red.[81] From our results, we can observe a shift toward the blue-green region (467–544 nm) on the La-doped CeO_2 sample in comparison to the pure sample, which is associated with the increase of shallow defects for the doped sample. Allied to the fact that La^{3+} promotes an increased stress along the c axis of the crystal structure with photon absorption close to 3 eV, as observed by UV–vis measurements,[46] these results indicate that the presence of singly ionized oxygen vacancies, $V_O^{\bullet}$, is maintained by the disordered state of the clusters in the structure, being characteristic of shallow defects,[82,83] in accordance with the sensing and magnetic behaviors explained above. The La-doped CeO_2 sample also shows emission in the infrared (IR) region, 762 nm, which is nonexistent in the undoped sample. The emission in the IR region is associated to sites of different symmetries with doping[84–86] While doping ceria with transition metals results in quenched effects on photoluminescent emission because of the reduction of defects, doping with La^{3+} increases the proportion of defects (Table 3), which results in high influence on the adsorption of gases on the surface.[87,88]

Table 3. XPS Measurements of the Pure and Lanthanum-Doped CeO_2 Sample before and after CO Exposure

sample	O_{defect}	$O_{lattice}$	$O_{defect}/O_{lattice}$	Ce^{3+}
$Ce_{1-(3/4)x}La_xO_2$	area	area	ratio	%
$X = 0.00$	20 423	91 066	0.22	23.88
$X = 0.08$	34 045	112 214	0.30	18.58
$X = 0.08$ (CO)	35 127	96 534	0.36	20.42

Once IR radiation can penetrate human tissues to differing extents depending on the wavelength range being used, this feature allows for its application in biomedical devices using LED arrays for mucositis prevention, wound healing, and tissue repair.[89] Besides being used for rhinitis, arthritis, and jaundice treatments, LEDs are also used for the relief of stress, seasonal affective, and biological clock disorders; not to mention their usage in the field of low-intensity photo-rejuvenation[90] as well as in fluorescence imaging and image-guided surgery.[91] A work reported by Smith et al.[92] showed the use of a 780 nm femtosecond laser as an "optical pacemaker" for heart muscle cells. Previous studies showed that distinct neural cells can be stimulated by IR-pulsed radiation.[93–95] In a 2002 article by Schieke et al.,[96] human dermal fibroblasts were exposed to IR radiation in the range of 760–1400 nm, from 10 to 60 min, showing an upregulation in the Matrix metalloproteinase 1 (MMP-1, the collagenase involved in the normal turnover of skin collagen). In this way, rare-earth doping opens up a wide range of possible applications regarding ceria-based nanomaterials.

https://dx.doi.org/10.1021/acsomega.9b04250
ACS Omega 2020, 5, 14879–14889

Besides, the addition of carbon monoxide can affect the formation of superficial defects in which the interaction of electrons and phonons in the lattice sites may lead to self-trapping. In such situation, the electrons polarize their neighboring molecules and become trapped in self-induced potential wells because of the polarization field generated by the moving electrons carried through the lattice. The treatment performed on the film in a reducing atmosphere like CO provided energy to a great number of electrons that were easily available for conduction, thereby changing the PL behavior. When the thick film is exposed to carbon monoxide, Figure 7c, some electrons, which are excited in the photoluminescent process absorb energy of photons ($h\nu$) and are promoted from the oxygen 2p states to lanthanum 3d, which results in the disappearance of the IR emission favoring the formation of intermediary energy levels within the band gap that no longer emits radiation in this particular wavelength.[97] Something that must be considered is that the disappearance of the IR emission with the introduction of CO can be associated to the decrease of self-trapped charges, less interaction between the electron and hole, and donor−acceptor recombination. Therefore, the whole system will be characterized by a distribution of deep and shallow defects mostly attributed to singly ionized oxygen vacancies, $V_O^{\bullet}$, and their defective complex clusters.[98]

A weak blue-green emission at 483 nm observed by Phoka et al.[99] was attributed to the excess of surface defects in CeO_2. Palard et al.[72] reported a strong UV emission near 400 nm and a weak blue signal at about 415 nm attributed to surface defects, as well as two supplementary weak bands probably attributed to charge transfer from O^{2-} to Ce^{4+}/Ce^{3+} species. Wang et al.[21] indicated that the emission bands ranging from 400 to 500 nm for CeO_2 are attributed to the hopping from different defect levels of the range from Ce 4f to O 2p band. Therefore, the luminescence bands ranging from 400 to 550 nm may be attributed to the transition from different defect levels to the VB. According to Martins and Isolani,[100] optical transitions of Ce 4f to Ce 5d are possible and result in more intense bands of transitions than Ce 4f to Ce 4f, which are usually very broad bands.

To better explain the origin of the photoluminescent contributions in the La-doped CeO_2 samples, the following arguments are proposed according to the X-ray photoemission spectroscopy (XPS) data evidenced in Table 3, depicted in Figure 7d. An increase of 8% in the proportion of defective to lattice-oxygen species as a consequence of La-doping is observed, likely ascribed to the creation of oxygen vacancies. This behavior can be depicted as if the lanthanum-doped CeO_2 sample presented 30% of vacant oxygen sites in its structure in the absence of CO, against 36% for the lanthanum-doped CeO_2 after CO exposure (La-doped CeO_2—CO). Besides, an increase of almost 2% in the number of Ce^{3+} species after CO exposure can be depicted, already suggesting the presence of defective species, such as Ce(III) species, likely responsible for the increased green-orange photoluminescent emission.

In this model, the magnitude and structural order−disorder effects determine the physical properties of the system, likely influenced by the equilibria of $[CeO_8]$ octahedral groups and their combination with defective neighboring species. Hence, distortion processes are triggered on rare-earth clusters, favoring the formation of intermediary energy levels within the band gap of the material, composed of mixed O 2p states along with La and Ce f-states (below the CB and slightly above the Fermi level). During the exposure to CO, some electrons are promoted from the O 2p states to higher energy levels through the absorption of energy. This mechanism results in the formation of self-trapped excitons, that is, trapping of electrons (e−) by holes ($h^{\bullet}$), generating polarons with electronic density that contributes to the magnetic and electrical behaviors. A photoemission ($h\nu$) occurs when electrons located in higher levels decay to an empty O 2p state. Thus, the proposed mechanism for photoluminescent emission is based on the distortion processes of defective clusters, such as $[CeO_8]'_O$, $[CeO_7{\cdot}V_O^{X}]$, $[CeO_7{\cdot}V_O^{\bullet}]$, and $[CeO_7{\cdot}V_O^{\bullet\bullet}]$, as well as to their wave−function interactions and the consequent cluster-to-cluster charge transfer (CCCT), as a result of CO exposure. Additionally, this behavior can also be associated with the formation of superficial defects caused by modifications on the morphology of the thick films[101] during synthesis steps and atmosphere exposure.

3. CONCLUSIONS

The photoluminescent, magnetic, and gas-sensing behaviors of rare earth-doped CeO_2 are strongly correlated to the creation of singly and doubly ionized oxygen vacancy species, which provokes the conversion of Ce^{4+} into Ce^{3+} and vice-versa, depending on the doping element as well as to the exposed atmosphere, opening up several possibilities of application regarding rare earth-modified cerium oxide. Quantitative phase analysis confirmed that the pure and lanthanum-doped cerium oxide samples could be well-indexed to a pure cubic structure of CeO_2 (space group: $Fm3m$), with lattice parameter a = 5.4165 Å. A fraction of the Ce species is in the +3 state, which explains the weak RT-FM of the sample ($M_s \approx 0.0068$ emu/g) being the ferromagnetic mechanism discussed by FCE. When the thick film is exposed to the CO atmosphere, some electrons are promoted from the oxygen 2p states to lanthanum/cerium f-states. Besides this, La^{3+} promotes increased stress along the c axis of the crystal lattice with photon absorption close to 2.31 eV, indicating that the disordered states of the clusters are responsible for maintaining shallow defects, particularly singly ionized oxygen vacancies ($V_O^{\bullet}$). Besides the magnetic and photoluminescent behavior, a fast response time (5.5 s) was observed after CO exposure, indicating that the defective structure of ceria-based materials corresponds to the key of success in terms of photoluminescent, magnetic, and electrical applications, owing to the transient $4f^1$ electrons that migrate by an activated tunneling/hopping mechanism of polarons intrinsically created by the redox processes when doped or exposed to an atmosphere.

4. EXPERIMENTAL PROCEDURES

4.1. Synthesis and Characterization of the CeO_2 Nanoparticles. $Ce_{1-(3/4)x}La_xO_2$ (x = 0.00 and 0.08) powders were synthesized by a MAH technique. A cerium(IV) nitrate hexahydrate $[Ce(NO_3)_3{\cdot}6H_2O$, 99.9%; Sigma-Aldrich] solution of 150 mM was prepared under constant stirring for 15 min at room temperature. The experimental procedure for the preparation of the $Ce_{1-(3/4)x}La_xO_2$ (x = 0.08) was based on dissolution of the cerium precursor in an aqueous medium under magnet stirring, and, separately, lanthanum oxide (La_2O_3, 99%; Sigma-Aldrich) was dissolved in distilled water with nitric acid and added to the former solution. The pH of the resulting mixture was adjusted to 10 using KOH (2 M,

https://dx.doi.org/10.1021/acsomega.9b04250
ACS Omega 2020, 5, 14879−14889

99.5%, Synth). The resulting solution was transferred into a sealed Teflon autoclave and placed in a microwave hydrothermal oven (2.45 GHz, 800 W). The system was heat treated at 100 °C for 8 min with a heating rate fixed at 10 °C/min, as previously published by our group.[10] The autoclave was cooled to room temperature naturally. The powders were centrifuged and washed with distilled water and then dried at 100 °C in an oven for 48 h. Powders were characterized using XRD with a PANalytical X'Pert PRO diffraction system employing Cu Kα radiation (λ = 0.1542 nm).[102] For Rietveld refinement, the following diffraction parameters were considered: 40 kV, 30 mA, $10° \leq 2\theta \geq 110°$, $\Delta 2\theta = 0.02°$, λCu Kα monocromatized by a graphite crystal, divergence slit = 2.0 mm, reception slit = 0.6 mm, and step time = 8 s. The Rietveld refinement method was calculated using the software GSAS (General Structure Analysis System)[103] and the graphic interface EXPGUI.[104] Samples for TEM were obtained by drying droplets of as-prepared samples from an ethanol dispersion, which was sonicated for 5 min onto 300 mesh Cu grids. TEM micrographs and selected area electron diffraction (SAED) analysis patterns were obtained at an accelerating voltage of 200 kV, on a FEI model Tecnai G2-20 instrument. Magnetization measurements were done by using a vibrating-sample magnetometer from Quantum Design.

4.2. Preparation and Characterization of the Thick Films. To obtain the lanthanum-doped cerium oxide thick films, a paste was prepared with an organic binder (glycerol) using the obtained powders. The used solid/organic binder ratio was 30 mg/0.05 mL. Thick porous films were conformed using the screen-printing technique onto the insulating alumina substrate, on which electrodes with an interdigitated shape had been delineated by sputtering. The insulating alumina substrates were 96% dense, with a 25 nm thick titanium layer deposited to improve adhesion, and a 175 nm thick platinum film deposited over the Ti-layer, both obtained with RF-sputtering at 5.10−3 bar, using 120 and 80 W. The interdigitated electrodes were defined in a home-built micromachining laser (l = 355 nm; f = 2 KHz). The resulting samples were thermally treated in a dry air atmosphere up to 60 °C for microscopy investigation. Next, the films were thermally treated up to 380 °C and maintained at this temperature for 2 h, using a heating rate of 1 °C/min to assure the elimination of organic compounds. The Raman spectroscopy characterization of the film before and after CO exposure was obtained by a LabRAM iHR550 Horiba Jobin Yvon spectrometer with a spectral resolution of 1 cm^{-1}, with 40 scans in the range of 100−1500 cm^{-1}, coupled to a CCD detector. The procedure was carried out with an argon-ion laser, whose wavelength is 514.5 nm and a power of 8 mW. The photoluminescent spectrum was obtained using thermal monochromator monospec27 Jarrel-Ash and a photomultiplier Hamamatsu R446. A laser (Coherent Innova) of wavelength 350.7 nm (2.57 eV), with 200 mW of power was used. All measurements were carried out at room temperature. The electrical resistance of the films was measured using an Agilent 3440A multimeter at different temperatures (25−450 °C), using a heating rate of 2° C/min, with respect to vacuum (10^{-3} mmHg or 1.33×10^{-6} bar), dry air (~20% O_2 with pressure of 50 mmHg), and CO (50 mmHg) atmospheres. In order to observe the film reversible behavior under atmosphere exposure, measurements of resistance versus time were carried out on the sample steady state, when a constant resistance was observed. The electric contribution regarding the used substrate and electrodes was already measured and published by Schipani et al.,[105] showing no significant influences to the overall response. The local binding structure and surface of the samples were investigated by X-ray photoemission spectroscopy (XPS) measurements, carried out in a Scienta Omicron ESCA + spectrometer system equipped with a hemispherical analyzer EA125 and a monochromatic source in Al Kα ($h\nu$ = 1486.7 eV). The source was used in 280 W, while the spectrometer worked on a constant energy rate mode of 50 eV. All data analysis was performed using CASA XPS Software (Casa Software Ltd, UK). A Shirley background subtraction was applied with the baseline encompassing the entire spectrum and correcting the charge effects using the C 1s peak at 285.0 eV as the charge reference.

AUTHOR INFORMATION

Corresponding Author

Leandro S.R. Rocha − *Department of Chemistry, Federal University of São Carlos (UFSCar), São Carlos, São Paulo 13565-905, Brazil;* orcid.org/0000-0002-6059-2197; Email: leandro.rocha@liec.ufscar.br

Authors

Rafael A.C. Amoresi − *School of Engineering, Sao Paulo State University (UNESP), Guaratinguetá, São Paulo 12516-410, Brazil;* orcid.org/0000-0002-7523-6013

Henrique Moreno − *School of Engineering, Sao Paulo State University (UNESP), Guaratinguetá, São Paulo 12516-410, Brazil*

Miguel A. Ramirez − *School of Engineering, Sao Paulo State University (UNESP), Guaratinguetá, São Paulo 12516-410, Brazil*

Miguel A. Ponce − *Institute of Materials Science and Technology Investigation (INTEMA), Mar del Plata 7600, Argentina*

Cesar R. Foschini − *School of Engineering, Sao Paulo State University (UNESP), Bauru, São Paulo 17033-360, Brazil*

Elson Longo − *Department of Chemistry, Federal University of São Carlos (UFSCar), São Carlos, São Paulo 13565-905, Brazil;* orcid.org/0000-0001-8062-7791

Alexandre Z. Simões − *School of Engineering, Sao Paulo State University (UNESP), Guaratinguetá, São Paulo 12516-410, Brazil*

Complete contact information is available at: https://pubs.acs.org/10.1021/acsomega.9b04250

Notes

The authors declare no competing financial interest.

ACKNOWLEDGMENTS

The authors acknowledge financial support of this research project by the Brazilian research funding agencies CNPq 573636/2008-7, INCTMN 2008/57872-1, and to FAPESP grant numbers 2013/07296-2, 2017/19143-7 and 2018/20590-0.

REFERENCES

(1) Anjana, P. S.; Sebastian, M. T. Low Dielectric Loss PTFE/CeO_2 Ceramic Composites for Microwave Substrate Applications. *Int. J. Appl. Ceram. Technol.* **2008**, *5*, 325−333.

(2) Koelling, D. D.; Boring, A. M.; Wood, J. H. The electronic structure of CeO_2 and PrO_2. *Solid State Commun.* **1983**, *47*, 227−232.

https://dx.doi.org/10.1021/acsomega.9b04250
ACS Omega 2020, 5, 14879−14889

(3) Li, R.; Yabe, S.; Yamashita, M.; Momose, S.; Yoshida, S.; Yin, S.; Sato, T. UV-shielding properties of zinc oxide-doped ceria fine powders derived via soft solution chemical routes. *Mater. Chem. Phys.* **2002**, *75*, 39−44.
(4) Xie, S.; Wang, Z.; Cheng, F.; Zhang, P.; Mai, W.; Tong, Y. Ceria and ceria-based nanostructured materials for photoenergy applications. *Nano Energy* **2017**, *34*, 313−337.
(5) Meng, T.; Ara, M.; Wang, L.; Naik, R.; Ng, K. Y. S. Enhanced capacity for lithium−air batteries using $LaFe_{0.5}Mn_{0.5}O_3$−CeO_2 composite catalyst. *J. Mater. Sci.* **2014**, *49*, 4058−4066.
(6) Bondioli, F.; Corradi, A. B.; Manfredini, T.; Leonelli, C.; Bertoncello, R. Nonconventional Synthesis of Praseodymium-Doped Ceria by Flux Method. *Chem. Mater.* **2000**, *12*, 324−330.
(7) Song, H.; Wang, H. B.; Zha, S. W.; Peng, D. K.; Meng, G. Y. Aerosol-assisted MOCVD growth of Gd_2O_3-doped CeO_2 thin SOFC electrolyte film on anode substrate. *Solid State Ionics* **2003**, *156*, 249−254.
(8) Thangadurai, V.; Kopp, P. Chemical synthesis of Ca-doped CeO_2 - Intermediate temperature oxide ion electrolytes. *J. Power Sources* **2007**, *168*, 178−183.
(9) Cavalcante, L. S.; Sczancoski, J. C.; Siu Li, M.; Longo, E.; Varela, J. A. β-$ZnMoO_4$ microcrystals synthesized by the surfactant-assisted hydrothermal method: Growth process and photoluminescence properties. *Colloids Surf., A* **2012**, *396*, 346−351.
(10) Deus, R. C.; Foschini, C. R.; Spitova, B.; Moura, F.; Longo, E.; Simões, A. Z. Effect of soaking time on the photoluminescence properties of cerium oxide nanoparticles. *Ceram. Int.* **2014**, *40*, 1−9.
(11) Dhara, A.; Sain, S.; Sadhukhan, P.; Das, S.; Pradhan, S. K. Effect of lattice distortion in optical properties of CeO_2 nanocrystals on Mn substitution by mechanical alloying. *J. Alloys Compd.* **2019**, *786*, 215−224.
(12) Abbas, F.; Jan, T.; Iqbal, J.; Haider Naqvi, M. S.; Ahmad, I. Inhibition of Neuroblastoma cancer cells viability by ferromagnetic Mn doped CeO_2 monodisperse nanoparticles mediated through reactive oxygen species. *Mater. Chem. Phys.* **2016**, *173*, 146−151.
(13) Liu, Y.; Lockman, Z.; Aziz, A.; MacManus-Driscoll, J. Size dependent ferromagnetism in cerium oxide (CeO_2) nanostructures independent of oxygen vacancies. *J. Phys.: Condens. Matter* **2008**, *20*, 165201.
(14) Chen, S.-Y.; Lu, Y.-H.; Huang, T.-W.; Yan, D.-C.; Dong, C.-L. Oxygen Vacancy Dependent Magnetism of CeO_2 Nanoparticles Prepared by Thermal Decomposition Method. *J. Phys. Chem. C* **2010**, *114*, 19576−19581.
(15) Ge, M. Y.; Wang, H.; Liu, E. Z.; Liu, J. F.; Jiang, J. Z.; Li, Y. K.; Xu, Z. A.; Li, H. Y. On the origin of ferromagnetism in CeO_2 nanocubes. *Appl. Phys. Lett.* **2008**, *93*, 062505.
(16) Lee, W.; Chen, S.-Y.; Tseng, E. N.; Gloter, A.; Ku, C.-W.; Li, X.-Y. Spectroscopic investigation of the correlation between localization of electrons and ferromagnetism in CeO_2 nanoparticles. *J. Magn. Magn. Mater.* **2018**, *464*, 11−17.
(17) Liu, B.; Liu, B.; Li, Q.; Li, Z.; Yao, M.; Liu, R.; Zou, X.; Lv, H.; Wu, W.; Cui, W.; Liu, Z.; Li, D.; Zou, B.; Cui, T.; Zou, G. High-pressure Raman study on CeO_2 nanospheres self-assembled by 5 nm CeO_2 nanoparticles. *Phys. Status Solidi B* **2011**, *248*, 1154−1157.
(18) Darroudi, M.; Sarani, M.; Kazemi Oskuee, R.; Khorsand Zak, A.; Hosseini, H. A.; Gholami, L. Green synthesis and evaluation of metabolic activity of starch mediated nanoceria. *Ceram. Int.* **2014**, *40*, 2041−2045.
(19) Nourmohammadi, E.; Kazemi Oskuee, R.; Hasanzadeh, L.; Mohajeri, M.; Hashemzadeh, A.; Rezayi, M.; Darroudi, M. Cytotoxic activity of greener synthesis of cerium oxide nanoparticles using carrageenan towards a WEHI 164 cancer cell line. *Ceram. Int.* **2018**, *44*, 19570−19575.
(20) Raubach, C. W.; Polastro, L.; Ferrer, M.; Perrin, A.; Perrin, C.; Albuquerque, A. R.; Buzolin, P.; Sambrano, J. R.; de Santana, Y. B. V.; Varela, J. A.; Longo, E. Influence of solvent on the morphology and photocatalytic properties of ZnS decorated CeO_2 nanoparticles. *J. Appl. Phys.* **2014**, *115*, 213514.
(21) Wang, G.; Mu, Q.; Chen, T.; Wang, Y. Synthesis, characterization and photoluminescence of CeO_2 nanoparticles by a facile method at room temperature. *J. Alloys Compd.* **2010**, *493*, 202−207.
(22) Andrievskaya, E. R.; Kornienko, O. A.; Sameljuk, A. V.; Sayir, A. Phase relation studies in the CeO_2−La_2O_3 system at 1100−1500°C. *J. Eur. Ceram. Soc.* **2011**, *31*, 1277−1283.
(23) Arul, N. S.; Mangalaraj, D.; Ramachandran, R.; Grace, A. N.; Han, J. I. Fabrication of CeO_2/Fe_2O_3 composite nanospindles for enhanced visible light driven photocatalysts and supercapacitor electrodes. *J. Mater. Chem. A* **2015**, *3*, 15248−15258.
(24) Sun, C.; Li, H.; Chen, L. Nanostructured ceria-based materials: synthesis, properties, and applications. *Energy Environ. Sci.* **2012**, *5*, 8475−8505.
(25) Shchukin, D. G.; Caruso, R. A. Template Synthesis and Photocatalytic Properties of Porous Metal Oxide Spheres Formed by Nanoparticle Infiltration. *Chem. Mater.* **2004**, *16*, 2287−2292.
(26) Goubin, F.; Rocquefelte, X.; Whangbo, M.-H.; Montardi, Y.; Brec, R.; Jobic, S. Experimental and Theoretical Characterization of the Optical Properties of CeO_2, $SrCeO_3$, and Sr_2CeO_4 Containing Ce^{4+} (f^0) Ions. *Chem. Mater.* **2004**, *16*, 662−669.
(27) Jasinski, P.; Suzuki, T.; Anderson, H. U. Nanocrystalline undoped ceria oxygen sensor. *Sens. Actuators, B* **2003**, *95*, 73−77.
(28) Sohlberg, K.; Pantelides, S. T.; Pennycook, S. J. Interactions of Hydrogen with CeO_2. *J. Am. Chem. Soc.* **2001**, *123*, 6609−6611.
(29) Yabe, S.; Yamashita, M.; Momose, S.; Tahira, K.; Yoshida, S.; Li, R.; Yin, S.; Sato, T. Synthesis and UV-shielding properties of metal oxide doped ceria via soft solution chemical processes. *Int. J. Inorg. Mater.* **2001**, *3*, 1003−1008.
(30) Jacobs, G.; Williams, L.; Graham, U.; Sparks, D.; Davis, B. H. Low-Temperature Water-Gas Shift: In-Situ DRIFTS−Reaction Study of a Pt/CeO2 Catalyst for Fuel Cell Reformer Applications. *J. Phys. Chem. B* **2003**, *107*, 10398−10404.
(31) Bera, P.; Gayen, A.; Hegde, M. S.; Lalla, N. P.; Spadaro, L.; Frusteri, F.; Arena, F. Promoting Effect of CeO_2 in Combustion Synthesized Pt/CeO_2 Catalyst for CO Oxidation. *J. Phys. Chem. B* **2003**, *107*, 6122−6130.
(32) Reddy, B. M.; Khan, A.; Yamada, Y.; Kobayashi, T.; Loridant, S.; Volta, J.-C. Raman and X-ray photoelectron spectroscopy study of CeO_2-ZrO_2 and V_2O_5/$CeOO_2$-ZrO_2 catalysts. *Langmuir* **2003**, *19*, 3025−3030.
(33) Li, D.; Tang, Y.; Ao, D.; Xiang, X.; Wang, S.; Zu, X. Ultra-highly sensitive and selective H_2S gas sensor based on CuO with sub-ppb detection limit. *Int. J. Hydrogen Energy* **2019**, *44*, 3985−3992.
(34) Li, D.; Zu, X.; Ao, D.; Tang, Q.; Fu, Y.; Guo, Y.; Bilawal, K.; Faheem, M. B.; Li, L.; Li, S.; Tang, Y. High humidity enhanced surface acoustic wave (SAW) H_2S sensors based on sol−gel CuO films. *Sens. Actuators, B* **2019**, *294*, 55−61.
(35) Wang, S.-Y.; Ma, J.-Y.; Li, Z.-J.; Su, H. Q.; Alkurd, N. R.; Zhou, W.-L.; Wang, L.; Du, B.; Tang, Y.-L.; Ao, D.-Y.; Zhang, S.-C.; Yu, Q. K.; Zu, X.-T. Surface acoustic wave ammonia sensor based on ZnO/SiO_2 composite film. *J. Hazard. Mater.* **2015**, *285*, 368−374.
(36) Bleecker, M. L. Carbon monoxide intoxication. *Occupational Neurology Handbook of Clinical Neurology*; Elsevier: Amsterdam, 2015; pp. 191−203.
(37) Kornyushchenko, A. S.; Jayatissa, A. H.; Natalich, V. V.; Perekrestov, V. I. Two step technology for porous ZnO nanosystem formation for potential use in hydrogen gas sensors. *Thin Solid Films* **2016**, *604*, 48−54.
(38) Wu, C.-H.; Zhu, Z.; Huang, S.-Y.; Wu, R.-J. Preparation of palladium-doped mesoporous WO_3 for hydrogen gas sensors. *J. Alloys Compd.* **2019**, *776*, 965−973.
(39) Mirzaei, A.; Park, S.; Kheel, H.; Sun, G.-J.; Lee, S.; Lee, C. ZnO-capped nanorod gas sensors. *Ceram. Int.* **2016**, *42*, 6187−6197.
(40) Mirzaei, A.; Neri, G. Microwave-assisted synthesis of metal oxide nanostructures for gas sensing application: A review. *Sens. Actuators, B* **2016**, *237*, 749−775.
(41) Wang, C.; Yin, L.; Zhang, L.; Xiang, D.; Gao, R. Metal Oxide Gas Sensor: Sensitivity and Influencing Factors. *Sensors* **2010**, *10*, 2088−2106.

https://dx.doi.org/10.1021/acsomega.9b04250
ACS Omega 2020, 5, 14879−14889

(42) Maekawa, T.; Suzuki, K.; Takada, T.; Kobayashi, T.; Egashira, M. Odor identification using a SnO_2-based sensor array. *Sens. Actuators, B* **2001**, *80*, 51−58.
(43) Barsan, N.; Weimar, U. Conduction Model of Metal Oxide Gas Sensors. *J. Electroceram.* **2001**, *7*, 143−167.
(44) Batzill, M.; Diebold, U. The surface and materials science of tin oxide. *Prog. Surf. Sci.* **2005**, *79*, 47−154.
(45) Zhu, L.; Zeng, W. Room-temperature gas sensing of ZnO-based gas sensor: A review. *Sens. Actuators, A* **2017**, *267*, 242−261.
(46) Rocha, L. S. R.; Cilense, M.; Ponce, M. A.; Aldao, C. M.; Oliveira, L. L.; Longo, E.; Simoes, A. Z. Novel gas sensor with dual response under CO(g) exposure: Optical and electrical stimuli. *Phys. B Condens. Matter* **2018**, *536*, 280−288.
(47) Lv, J.; Fang, M.; Liu, Y. Oxygen-exposure mediated electron transfer and d^0 ferromagnetism in metal oxide nanocrystals system. *J. Alloys Compd.* **2017**, *721*, 633−637.
(48) Farrukh, M. A.; Butt, K. M.; Chong, K.-K.; Chang, W. S. Photoluminescence emission behavior on the reduced band gap of Fe doping in CeO_2-SiO_2 nanocomposite and photophysical properties. *J. Saudi Chem. Soc.* **2019**, *23*, 561−575.
(49) Souza, A. E.; Sasaki, G. S.; Camacho, S. A.; Teixeira, S. R.; Li, M. S.; Longo, E. Defects or charge transfer : Different possibilities to explain the photoluminescence in crystalline $Ba(Zr_xTi_{1-x})O_3$. *J. Lumin.* **2016**, *179*, 132−138.
(50) Du, D.; Kullgren, J.; Hermansson, K.; Broqvist, P. From Ceria Clusters to Nanoparticles: Superoxides and Supercharging. *J. Phys. Chem. C* **2019**, *123*, 1742−1750.
(51) Brauer, G.; Gingerich, K. A. Über die oxyde des cers—V: Hochtemperatur-Röntgenuntersuchungen an ceroxyden. *J. Inorg. Nucl. Chem.* **1960**, *16*, 87−99.
(52) Meyer, G.; Morss, L. R. *Synthesis of Lanthanide and Actinide Compounds*; Springer: Dordrecht, 1991.
(53) Liang, S.; Broitman, E.; Wang, Y.; Cao, A.; Veser, G. Highly stable, mesoporous mixed lanthanum−cerium oxides with tailored structure and reducibility. *J. Mater. Sci.* **2011**, *46*, 2928−2937.
(54) Miki, T.; Ogawa, T.; Haneda, M.; Kakuta, N.; Ueno, A.; Tateishi, S.; Matsuura, S.; Sato, M. Enhanced oxygen storage capacity of cerium oxides in cerium dioxide/lanthanum sesquioxide/alumina containing precious metals. *J. Phys. Chem.* **1990**, *94*, 6464−6467.
(55) Kao, K. C. Electrical Conduction and Photoconduction. *Dielectric Phenomena in Solids*; Academic Press: San Diego, 2004; pp 381−514.
(56) Deus, R. C.; Cilense, M.; Foschini, C. R.; Ramirez, M. A.; Longo, E.; Simões, A. Z. Influence of mineralizer agents on the growth of crystalline CeO_2 nanospheres by the microwave-hydrothermal method. *J. Alloys Compd.* **2013**, *550*, 245−251.
(57) Murugan, R.; Vijayaprasath, G.; Thangaraj, M.; Mahalingam, T.; Rajendran, S.; Arivanandhan, M.; Loganathan, A.; Hayakawa, Y.; Ravi, G. Defect assisted room temperature ferromagnetism on rf sputtered Mn doped CeO_2 thin films. *Ceram. Int.* **2017**, *43*, 399−406.
(58) Dimri, M. C.; Khanduri, H.; Kooskora, H.; Subbi, J.; Heinmaa, I.; Mere, A.; Krustok, J.; Stern, R. Ferromagnetism in rare-earth doped cerium oxide bulk samples. *Phys. Status Solidi A* **2012**, *209*, 353−358.
(59) Sundaresan, A.; Bhargavi, R.; Rangarajan, N.; Siddesh, U.; Rao, C. N. R. Ferromagnetism as a universal feature of nanoparticles of the otherwise nonmagnetic oxides. *Phys. Rev. B: Condens. Matter Mater. Phys.* **2006**, *74*, 161306.
(60) Kumar, S.; Kim, Y. J.; Koo, B. H.; Lee, C. G. Structural and Magnetic Properties of Ni Doped CeO_2 Nanoparticles. *J. Nanosci. Nanotechnol.* **2010**, *10*, 7204−7207.
(61) Coey, J. M. D.; Douvalis, A. P.; Fitzgerald, C. B.; Venkatesan, M. Ferromagnetism in Fe-doped SnO_2 thin films. *Appl. Phys. Lett.* **2004**, *84*, 1332−1334.
(62) Esch, F.; Fabris, S.; Zhou, L.; Montini, T.; Africh, C.; Fornasiero, P.; Comelli, G.; Rosei, R. Electron Localization Determines Defect Formation on Ceria Substrates. *Science* **2005**, *309*, 752−755.
(63) Dutta, D. P.; Tyagi, A. K. Novel Features of Multiferroic Materials. *BARC Newsl.* **2013**, *335*, 48−54.
(64) Weber, W. H.; Hass, K. C.; McBride, J. R. Raman study of CeO_2: Second-order scattering, lattice dynamics, and particle-size effects. *Phys. Rev. B: Condens. Matter Mater. Phys.* **1993**, *48*, 178−185.
(65) Iglesias, I.; Baronetti, G.; Mariño, F. Ceria and $Ce_{0.95}M_{0.05}O_{2-\delta}$ mixed oxides (M=La, Pr, Zr): Vacancies and reducibility study. *Solid State Ionics* **2017**, *309*, 123−129.
(66) He, D.; Hao, H.; Chen, D.; Liu, J.; Yu, J.; Lu, J.; Liu, F.; Wan, G.; He, S.; Luo, Y. Synthesis and application of rare-earth elements (Gd, Sm, and Nd) doped ceria-based solid solutions for methyl mercaptan catalytic decomposition. *Catal. Today* **2017**, *281*, 559−565.
(67) Ortega, P. P.; Rocha, L. S. R.; Cortés, J. A.; Ramirez, M. A.; Buono, C.; Ponce, M. A.; Simões, A. Z. Towards carbon monoxide sensors based on europium doped cerium dioxide. *Appl. Surf. Sci.* **2019**, *464*, 692−699.
(68) Schilling, C.; Hofmann, A.; Hess, C.; Ganduglia-Pirovano, M. V. Raman Spectra of Polycrystalline CeO_2: A Density Functional Theory Study. *J. Phys. Chem. C* **2017**, *121*, 20834−20849.
(69) Pushkarev, V. V.; Kovalchuk, V. I.; d'Itri, J. L. Probing Defect Sites on the CeO_2 Surface with Dioxygen. *J. Phys. Chem. B* **2004**, *108*, 5341−5348.
(70) Dos Santos, M. L.; Lima, R. C.; Riccardi, C. S.; Tranquilin, R. L.; Bueno, P. R.; Varela, J. A.; Longo, E. Preparation and characterization of ceria nanospheres by microwave-hydrothermal method. *Mater. Lett.* **2008**, *62*, 4509−4511.
(71) Zawadzki, M. Preparation and characterization of ceria nanoparticles by microwave-assisted solvothermal process. *J. Alloys Compd.* **2008**, *454*, 347−351.
(72) Palard, M.; Balencie, J.; Maguer, A.; Hochepied, J.-F. Effect of hydrothermal ripening on the photoluminescence properties of pure and doped cerium oxide nanoparticles. *Mater. Chem. Phys.* **2010**, *120*, 79−88.
(73) Deus, R. C.; Cortés, J. A.; Ramirez, M. A.; Ponce, M. A.; Andres, J.; Rocha, L. S. R.; Longo, E.; Simões, A. Z. Photoluminescence properties of cerium oxide nanoparticles as a function of lanthanum content. *Mater. Res. Bull.* **2015**, *70*, 416−423.
(74) Shankar, P.; Bosco, J.; Rayappan, B. Gas sensing mechanism of metal oxides: The role of ambient atmosphere, type of semiconductor and gases - A review. *Sci. Lett. J.* **2015**, *4*, 126.
(75) Durrani, S. M. A.; Al-Kuhaili, M. F.; Bakhtiari, I. A. Carbon monoxide gas-sensing properties of electron-beam deposited cerium oxide thin films. *Sens. Actuators, B* **2008**, *134*, 934−939.
(76) Izu, N.; Itoh, T.; Nishibori, M.; Matsubara, I.; Shin, W. Effects of noble metal addition on response of ceria thick film CO sensors. *Sens. Actuators, B* **2012**, *171−172*, 350−353.
(77) Izu, N.; Nishizaki, S.; Itoh, T.; Nishibori, M.; Shin, W.; Matsubara, I. Gas response, response time and selectivity of a resistive CO sensor based on two connected CeO_2 thick films with various particle sizes. *Sens. Actuators, B* **2009**, *136*, 364−370.
(78) López-Mena, E. R.; Michel, C. R.; Martínez-Preciado, A. H.; Elías-Zuñiga, A. Simple Route to Obtain Nanostructured CeO_2 Microspheres and CO Gas Sensing Performance. *Nanoscale Res. Lett.* **2017**, *12*, 169.
(79) Souza, A. E.; Santos, G. T. A.; Barra, B. C.; Macedo, W. D.; Teixeira, S. R.; Santos, C. M.; Senos, A. M. O. R.; Amaral, L.; Longo, E. Photoluminescence of $SrTiO_3$: Influence of Particle Size and Morphology. *Cryst. Growth Des.* **2012**, *12*, 5671−5679.
(80) Kan, D.; Masuno, A. Blue-Light Emission at Room Temperature from Ar+-Irradiated $SrTiO_3$. *Nat. Mater.* **2005**, *4*, 816−819.
(81) Pan, X.; Yang, M.-Q.; Fu, X.; Zhang, N.; Xu, Y.-J. Defective TiO_2 with oxygen vacancies: synthesis, properties and photocatalytic applications. *Nanoscale* **2013**, *5*, 3601−3614.
(82) Li, H.; Guo, Y.; Robertson, J. Calculation of TiO_2 Surface and Subsurface Oxygen Vacancy by the Screened Exchange Functional. *J. Phys. Chem. C* **2015**, *119*, 18160−18166.
(83) Amoresi, R. A. C.; Teodoro, V.; Teixeira, G. F.; Li, M. S.; Simões, A. Z.; Perazolli, L. A.; Longo, E.; Zaghete, M. A. Electrosteric colloidal stabilization for obtaining $SrTiO_3/TiO_2$ heterojunction:

https://dx.doi.org/10.1021/acsomega.9b04250
ACS Omega 2020, 5, 14879−14889

Microstructural evolution in the interface and photonics properties. *J. Eur. Ceram. Soc.* **2018**, *38*, 1621−1631.
(84) Sun, C.; Xue, D. The synergy effect of rare earth cations on local structure and PL emission in a Ce^{3+}:$REPO_4$ (RE = La, Gd, Lu, Y) system. *Dalton Trans.* **2017**, *46*, 7888−7896.
(85) Coleto, U.; Amoresi, R. A. C.; Pereira, C. A. M.; Simões, A. Z.; Zaghete, M. A.; Monteiro Filho, E. S.; Longo, E.; Perazolli, L. A. Influence of defects on photoluminescent and photocatalytic behavior of CaO/$SrTiO_3$ heterojunctions. *Ceram. Int.* **2019**, *45*, 15244−15251.
(86) Vequizo, J. J. M.; Kamimura, S.; Ohno, T.; Yamakata, A. Oxygen induced enhancement of NIR emission in brookite TiO_2 powders: comparison with rutile and anatase TiO_2 powders. *Phys. Chem. Chem. Phys.* **2018**, *20*, 3241−3248.
(87) Sani, Z. K.; Ghodsi, F. E.; Mazloom, J. Surface morphology effects on Li ion diffusion toward CeO_2:Cu nanostructured thin films incorporated in PEG matrix. *J. Sol-Gel Sci. Technol.* **2017**, *82*, 643−653.
(88) Zamiri, R.; Salehizadeh, S. A.; Ahangar, H. A.; Shabani, M.; Rebelo, A.; Ferreira, J. M. F. Dielectric and optical properties of Ni- and Fe-doped CeO_2 nanoparticles. *Appl. Phys. A* **2019**, *125*, 393.
(89) Desmet, K. D.; Paz, D. A.; Corry, J. J.; Eells, J. T.; Wong-riley, M. T. T.; Henry, M. M.; Buchmann, E. V.; Connelly, M. P.; Dovi, J. V.; Liang, H. L.; Henshel, D. S.; Yeager, R. L.; Millsap, D. S.; Millsap, D. S.; Lim, J.; Gould, L. J.; Das, R.; Jett, M.; Hodgson, B. D.; Margolis, D.; Whelan, H. T. Clinical and Experimental Applications of NIR-LED Photobiomodulation, Photomed. *Lasers Surg.* **2006**, *24*, 121−128.
(90) Gary, N.; Wu, C.; Chih, T. Light-emitting diodes — Their potential in biomedical applications. *Renew. Sustain. Energy Rev.* **2010**, *14*, 2161−2166.
(91) Gioux, S.; Ciocan, R. Engineers, E. High Power, Computer-Controlled, LED-Based Light Sources for Fluorescence Imaging and Image-Guided Surgery. *Mol. Imag.* **2009**, *8*, 7290−2009.
(92) Smith, N. I.; Kumamoto, Y.; Iwanaga, S.; Ando, J.; Fujita, K.; Kawata, S. A femtosecond laser pacemaker for heart muscle cells. *Opt. Express* **2008**, *16*, 8604.
(93) Dittami, G. M.; Rajguru, S. M.; Lasher, R. A.; Hitchcock, R. W.; Rabbitt, R. D. Intracellular calcium transients evoked by pulsed infrared radiation in neonatal cardiomyocytes. *J. Physiol.* **2011**, *589*, 1295−1306.
(94) Wells, J.; Mahadevan-jansen, A. Application of infrared light for in vivo neural stimulation. *J. Biomed. Optic.* **2005**, *10*, 064003.
(95) Littlefield, P. D.; Vujanovic, I.; Mundi, J.; Matic, A. I.; Richter, C.-P. Laser Stimulation of Single Auditory Nerve Fibers. *Laryngoscope* **2010**, *120*, 2071−2082.
(96) Schieke, S. M.; Stege, H.; Kürten, V.; Grether-Beck, S.; Sies, H.; Krutmann, J. Infrared-A Radiation-Induced Matrix Metalloproteinase 1 Expression is Mediated Through Extracellular Signal-regulated Kinase 1/2 Activation in Human Dermal Fibroblasts. *J. Invest. Dermatol.* **2002**, *119*, 1323−1329.
(97) Mondego, M.; de Oliveira, R. C.; Penha, M.; Li, M. S.; Longo, E. Blue and red light photoluminescence emission at room temperature from $CaTiO_3$ decorated with α-Ag_2WO_4. *Ceram. Int.* **2017**, *43*, 5759−5766.
(98) Longo, V. M.; de Figueiredo, A. T.; de Lázaro, S.; Gurgel, M. F.; Costa, M. G. S.; Paiva-Santos, C. O.; Varela, J. A.; Longo, E.; Mastelaro, V. R.; DE Vicente, F. S.; Hernandes, A. C.; Franco, R. W. A. Structural conditions that leads to photoluminescence emission in SrTiO3: An experimental and theoretical approach. *J. Appl. Phys.* **2008**, *104*, 023515.
(99) Phoka, S.; Laokul, P.; Swatsitang, E.; Promarak, V.; Seraphin, S.; Maensiri, S. Synthesis, structural and optical properties of CeO_2 nanoparticles synthesized by a simple polyvinyl pyrrolidone (PVP) solution route. *Mater. Chem. Phys.* **2009**, *115*, 423−428.
(100) Martins, T. S.; Isolani, P. C. Terras raras: Aplicações industriais e biológicas. *Quim. Nova* **2005**, *28*, 111−117.
(101) Oliveira, L. H.; Paris, E. C.; Avansi, W.; Ramirez, M. A.; Mastelaro, V. R.; Longo, E.; Varela, J. A. Correlation Between Photoluminescence and Structural Defects in Ca^{1+}. *J. Am. Ceram. Soc.* **2013**, *96*, 209−217.
(102) Young, R. A.; Sakthivel, A.; Moss, T. S.; Paiva-Santos, C. O. DBWS-9411 - an upgrade of the DBWS*.* programs for Rietveld refinement with PC and main- frame computers. *J. Appl. Crystallogr.* **1995**, *28*, 366−367.
(103) Larson, A. C. General Structure Analysis System (GSAS). *Los Alamos Lab. Rep.* **1994**, *748*, 86−748.
(104) Toby, B. H. EXPGUI , a graphical user interface for GSAS. *J. Appl. Crystallogr.* **2001**, *34*, 210−213.
(105) Schipani, F.; Ponce, M. A.; Joanni, E.; Williams, F. J.; Aldao, C. M. Study of the oxygen vacancies changes in SnO_2 polycrystalline thick films using impedance and photoemission spectroscopies. *J. Appl. Phys.* **2014**, *116*, 194502.

https://dx.doi.org/10.1021/acsomega.9b04250
ACS Omega 2020, 5, 14879−14889